

University of Groningen

The Stars of the HETDEX Survey. I. Radial Velocities and Metal-Poor Stars from Low-Resolution Stellar Spectra

Hawkins, Keith; Zeimann, Greg; Sneden, Chris; Mentuch Cooper, Erin; Gebhardt, Karl; Bond, Howard E.; Carrillo, Andreia; Casey, Caitlin M.; Castanheira, Barbara G.; Ciardullo, Robin

Published in:
The Astrophysical Journal

DOI:
[10.3847/1538-4357/abe9bd](https://doi.org/10.3847/1538-4357/abe9bd)

IMPORTANT NOTE: You are advised to consult the publisher's version (publisher's PDF) if you wish to cite from it. Please check the document version below.

Document Version
Publisher's PDF, also known as Version of record

Publication date:
2021

[Link to publication in University of Groningen/UMCG research database](#)

Citation for published version (APA):

Hawkins, K., Zeimann, G., Sneden, C., Mentuch Cooper, E., Gebhardt, K., Bond, H. E., Carrillo, A., Casey, C. M., Castanheira, B. G., Ciardullo, R., Davis, D., Farrow, D. J., Finkelstein, S. L., Hill, G. J., Kelz, A., Liu, C., Shetrone, M., Schneider, D. P., Starkenburg, E., ... Wheeler, C. (2021). The Stars of the HETDEX Survey. I. Radial Velocities and Metal-Poor Stars from Low-Resolution Stellar Spectra. *The Astrophysical Journal*, 911(2), [108]. <https://doi.org/10.3847/1538-4357/abe9bd>

Copyright

Other than for strictly personal use, it is not permitted to download or to forward/distribute the text or part of it without the consent of the author(s) and/or copyright holder(s), unless the work is under an open content license (like Creative Commons).

The publication may also be distributed here under the terms of Article 25fa of the Dutch Copyright Act, indicated by the "Taverne" license. More information can be found on the University of Groningen website: <https://www.rug.nl/library/open-access/self-archiving-pure/taverne-amendment>.















Take-down policy

If you believe that this document breaches copyright please contact us providing details, and we will remove access to the work immediately and investigate your claim.

Downloaded from the University of Groningen/UMCG research database (Pure): <http://www.rug.nl/research/portal>. For technical reasons the number of authors shown on this cover page is limited to 10 maximum.



The Stars of the HETDEX Survey. I. Radial Velocities and Metal-poor Stars from Low-resolution Stellar Spectra

Keith Hawkins¹ , Greg Zeimann² , Chris Sneden¹ , Erin Mentuch Cooper¹ , Karl Gebhardt¹ , Howard E. Bond^{3,4} ,
Andraia Carrillo¹, Caitlin M. Casey¹ , Barbara G. Castanheira^{5,6}, Robin Ciardullo^{3,7} , Dustin Davis¹, Daniel J. Farrow⁸,
Steven L. Finkelstein¹ , Gary J. Hill^{1,6} , Andreas Kelz⁹, Chenxu Liu¹, Matthew Shetrone¹⁰ , Donald P. Schneider^{3,7} ,
Else Starkenburg^{9,11}, Matthias Steinmetz⁹ , and J. Craig Wheeler¹ 
(The HETDEX Collaboration)

¹ Department of Astronomy, The University of Texas at Austin, 2515 Speedway Boulevard, Austin, TX 78712, USA; keithhawkins@utexas.edu

² Hobby Eberly Telescope, University of Texas, Austin, TX, 78712, USA

³ Department of Astronomy & Astrophysics, The Pennsylvania State University, University Park, PA 16802, USA

⁴ Space Telescope Science Institute, 3700 San Martin Drive, Baltimore, MD 21218, USA

⁵ Department of Physics, Baylor University, One Bear Place #97316 Waco, TX 76798-7316, USA

⁶ McDonald Observatory, The University of Texas at Austin, 2515 Speedway Boulevard, Austin, TX 78712, USA

⁷ Institute for Gravitation and the Cosmos, The Pennsylvania State University, University Park, PA 16802, USA

⁸ Max-Planck-Institut für extraterrestrische Physik, Postfach 1312 Giessenbachstrasse, D-85741 Garching, Germany

⁹ Leibniz-Institut für Astrophysik Potsdam (AIP), An der Sternwarte 16, D-14482 Potsdam, Germany

¹⁰ UC Observatories UC Santa Cruz 1156 High Street Santa Cruz, CA 95064, USA

¹¹ Kapteyn Astronomical Institute, University of Groningen, Landleven 12, 9747 AD Groningen, The Netherlands

Received 2020 September 18; revised 2021 February 11; accepted 2021 February 11; published 2021 April 22

Abstract

The Hobby–Eberly Telescope Dark Energy Experiment (HETDEX) is an unbiased, massively multiplexed spectroscopic survey, designed to measure the expansion history of the universe through low-resolution ($R \sim 750$) spectra of Ly α emitters. In its search for these galaxies, HETDEX will also observe a few times 10^5 stars. In this paper, we present the first stellar value-added catalog within the internal second data release of the HETDEX Survey (HDR2). The new catalog contains 120,571 low-resolution spectra for 98,736 unique stars between $10 < G < 22$ spread across the HETDEX footprint at relatively high ($b \sim 60^\circ$) Galactic latitudes. With these spectra, we measure radial velocities (RVs) for $\sim 42,000$ unique FGK-type stars in the catalog and show that the HETDEX spectra are sufficient to constrain these RVs with a 1σ precision of 28.0 km s^{-1} and bias of 3.5 km s^{-1} with respect to the Large Sky Area Multi-Object Fibre Spectroscopic Telescope surveys and 1σ precision of 27.5 km s^{-1} and bias of 14.0 km s^{-1} compared to the Sloan Extension for Galactic Understanding and Exploration survey. Since these RVs are for faint ($G \geq 16$) stars, they will be complementary to Gaia. Using t-Distributed Stochastic Neighbor Embedding (tSNE), we also demonstrate that the HETDEX spectra can be used to determine a star’s T_{eff} , and $\log g$ and its $[\text{Fe}/\text{H}]$. With the tSNE projection of the FGK-type stars with HETDEX spectra we also identify 416 new candidate metal-poor ($[\text{Fe}/\text{H}] < -1$ dex) stars for future study. These encouraging results illustrate the utility of future low-resolution stellar spectroscopic surveys.

Unified Astronomy Thesaurus concepts: [Stellar types \(1634\)](#); [Catalogs \(205\)](#); [Surveys \(1671\)](#)

Supporting material: machine-readable table

1. Introduction

One of the primary goals within Galactic astronomy is to constrain the nature of the physical processes that govern how the Milky Way formed, assembled, and evolved from its birth to today. The key observational data that constrain theories of Milky Way formation include the position, velocities, and stellar atmospheric parameters for millions of stars across the Galaxy. This is what has given rise to missions such as Gaia, which have enabled the detailed study of the positions and velocities for ~ 1.7 billion stars through precise astrometric data (Gaia Collaboration et al. 2018), and has also been a key driver for the creation of large multi-object stellar spectroscopic surveys. Stellar spectra, whether at low or high resolution,¹² are particularly useful because they enable not only measurement of the radial velocity (RV) of stars, giving us 3D velocity information when combined with Gaia, but also they contain

critical information, including the effective temperature (T_{eff}), surface gravity ($\log g$), metallicity ($[\text{Fe}/\text{H}]$), and chemical abundance ratios ($[\text{X}/\text{Fe}]$), for large samples of stars.

Large spectroscopic surveys have been instrumental in uncovering the history and nature of our the Milky Way and beyond. These projects have obtained data which range from low to high resolution. For example, while the primary goal of the original the Sloan Digital Sky Survey (SDSS; York et al. 2000) was to map galaxies and quasars across the universe, the survey also obtained low-resolution ($R \sim 2000$) spectra for $\sim 10^5$ stars through the Sloan Extension for Galactic Understanding and Exploration (SEGUE; Yanny et al. 2009). Similar to SEGUE, the most recent data release (DR5) from the Large Sky Area Multi-Object Fibre Spectroscopic Telescope survey (LAMOST DR5; Luo et al. 2015; Xiang et al. 2017) contains low-resolution ($R \sim 1800$) spectra for over eight million stars. At moderate resolution ($R \sim 7500$), the magnitude-limited Radial Velocity Experiment (RAVE; Steinmetz et al. 2006, 2020),

¹² Resolving power is defined as $R = \lambda/\Delta\lambda$.

whose aim was to explore the structure and nature of the Milky Way, observed more than half a million stars observed in the southern hemisphere and derive not only RV information but also stellar atmospheric parameters for their sample.

Moving toward higher resolution the GALactic Archaeology with HERMES (GALAH; De Silva et al. 2015; Buder et al. 2018) survey has obtained optical spectra of 342,682 stars at $R \sim 28,000$, the SDSS-IV Apache Point Observatory Galactic Evolution Experiment (APOGEE; Majewski et al. 2017; Ahumada et al. 2020, H. Jönsson et al. 2021, in preparation) survey has collected infrared (H -band) spectra for upwards of 400,000 stars at $R \sim 21,000$, and the Gaia-ESO survey (Gilmore et al. 2012) aims to collect up to 100,000 spectra at $R \sim 47,000$. As one moves toward higher resolution, sample sizes decrease because of the tradeoff that exists between the resolution of the spectrograph and the exposure time required to obtain high signal-to-noise ratio (S/N) data required for the scientific aims of the surveys.

With high resolution, it is possible to derive both the detailed stellar atmospheric parameters (T_{eff} , $\log g$, $[\text{Fe}/\text{H}]$) and the chemical abundance ratios, denoted as $[\text{X}/\text{Fe}]$, for many elements. This is the case for surveys like APOGEE, GALAH, and Gaia-ESO. However, for lower-resolution spectroscopic surveys (e.g., SDSS, LAMOST), it becomes significantly more challenging to recover the stellar parameters and detailed chemical fingerprint. In fact, until recently, many low-resolution surveys only were able to determine the T_{eff} , $\log g$, $[\text{Fe}/\text{H}]$ and, in some cases, $[\alpha/\text{Fe}]$ ¹³ (e.g., Lee et al. 2008a, 2015; Boeche et al. 2018). Despite this limitation, Ting et al. (2017) demonstrated that it may be possible to measure not only the stellar atmospheric parameters but also several key individual elements down to $R \gtrsim 700$ with precisions at the ~ 0.15 dex level. While, at first, the results from these authors seem surprising, Xiang et al. (2019) illustrated the power of new machine learning techniques and derived the stellar parameters and 16 $[\text{X}/\text{Fe}]$ atmospheric abundance ratios from the low-resolution ($R \sim 1800$) LAMOST spectra. Additionally, other works have shown that it is possible to uncover metal-poor stars from low-resolution ($R < 1000$) spectra (e.g., Aguado et al. 2019) and even from photometry (e.g., Starkenburg et al. 2017; Casagrande et al. 2019; Lucey et al. 2019).

These new low-resolution techniques offer many opportunities including discovering and characterizing relatively rare, yet scientifically important, metal-poor stars. Metal-poor stars, defined as those with $[\text{Fe}/\text{H}] < -1.0$ dex, are important because they offer insights into the early Galaxy as well as constrain the nucleosynthesis of the elements (e.g. Bromm & Larson 2004; Beers & Christlieb 2005; Karlsson et al. 2013; Yong et al. 2013; Roederer et al. 2014; Frebel & Norris 2015; Sakari et al. 2018, and references therein). These stars are pretty rare yet their chemical properties are highly sought after. Hunting metal-poor stars, especially those at the lowest metallicities, is still a critical task. Several low- to medium-resolution surveys have been instrumental in finding and characterizing these metal-poor stars (e.g., Aoki et al. 2008; Ruchti et al. 2010; Xu et al. 2013; Matijević et al. 2017; Li et al. 2018).

In this context, the Hobby-Eberly Telescope Dark Energy Experiment (HETDEX; Hill et al. 2008, 2016, K. Gebhardt et al. 2021, in preparation) is a low-resolution

($R \sim 750$) *blind* spectroscopic survey whose primary goal is to map the locations and redshifts of high- z Ly α -emitting galaxies to constrain the nature of dark energy. This survey will cover a total of ~ 450 sq. deg. However, much like the case for SDSS, which was designed for cosmological investigations but eventually observed many stars, HETDEX will obtain spectra for large numbers of stars in its search for Ly α emitters. The unbiased nature of HETDEX (i.e., no preselection of objects is done), makes it extremely powerful, when compared to other large stellar spectroscopic surveys, to answer questions about the properties of the Milky Way. Therefore, we explore the use of these low-resolution HETDEX data for stellar astrophysics applications, such as deriving radial velocities for faint stars in the Gaia catalog and finding rare, but scientifically critical, metal-poor stars using machine learning. This is the first time these techniques have been applied to this data set.

This paper is structured as follows: Section 2 details the spectroscopic data collected from the HETDEX survey and presents the HETDEX-Gaia value-added catalog. We also describe the overlap data set used to validate our methods. In Section 3 we describe the methods used to constrain the RVs for the FGK-type stars found in the HETDEX survey and the t-distributed Stochastic Neighbor Embedding (tSNE) machine-learning method that we used to uncover candidate metal-poor stars. Section 4 presents the results of the RV and tSNE analysis and discusses the role HETDEX may play in constraining the nature of the Galaxy. Finally, in Section 5 we summarize our results and describe several future possible investigations with the data presented here.

2. Data

2.1. The HETDEX Survey

The HETDEX survey, which aims to constrain the nature of dark energy by observing Ly α emitters in the redshift interval $1.9 \leq z \leq 3.5$, is currently being carried out on the Hobby-Eberly Telescope (HET; Ramsey et al. 1994), which is an 11 m telescope with a segmented primary mirror, recently upgraded with a 22' field of view and 10 m pupil (Hill et al. 2018a). The upgraded HET includes a key new instrument called the Visible Integral-field Replicable Unit Spectrograph (VIRUS; Hill 2014; Hill et al. 2018b), which is a massively replicated, fiber-fed integral field spectrograph designed specifically to perform unbiased spectroscopic surveys. The entire VIRUS instrument consists of up to 156 integral field low-resolution (resolving power $R \sim 750$) spectrographs, arrayed in 78 pairs. Each of the 78 VIRUS units is fed by 448 1''5 fibers. Each of the fibers is fed to individual spectrographs (two per IFU) and dispersed onto CCD detectors at a mostly equal spacing on the detector. The spectrographs have a fixed spectral window in the optical with $3500 < \lambda < 5500 \text{ \AA}$ with 2 Å pixels. This represents a pixel size of $\sim 130 \text{ km s}^{-1}$. At full deployment,¹⁴ VIRUS will be able to capture 34,944 spectra for each exposure. The instrumentation for HETDEX is described in G. J. Hill et al. (2021, in preparation). The HETDEX survey, which is currently underway with the VIRUS instrument, will be a *blind* emission line survey of an area on the sky

¹³ In this case, $[\alpha/\text{Fe}]$ represents the average abundance ratio of $[\text{X}/\text{Fe}]$ the *alpha* elements (i.e., $\text{X} = [\text{Mg}, \text{Si}, \text{Ca}, \dots]$).

¹⁴ The VIRUS units have been deployed on the HET one-by-one, beginning in 2015. As of writing, 74 of the 78 units are currently active. The data from this paper were collected over the period 2017 January–2020 June with between 16 and 71 units deployed.

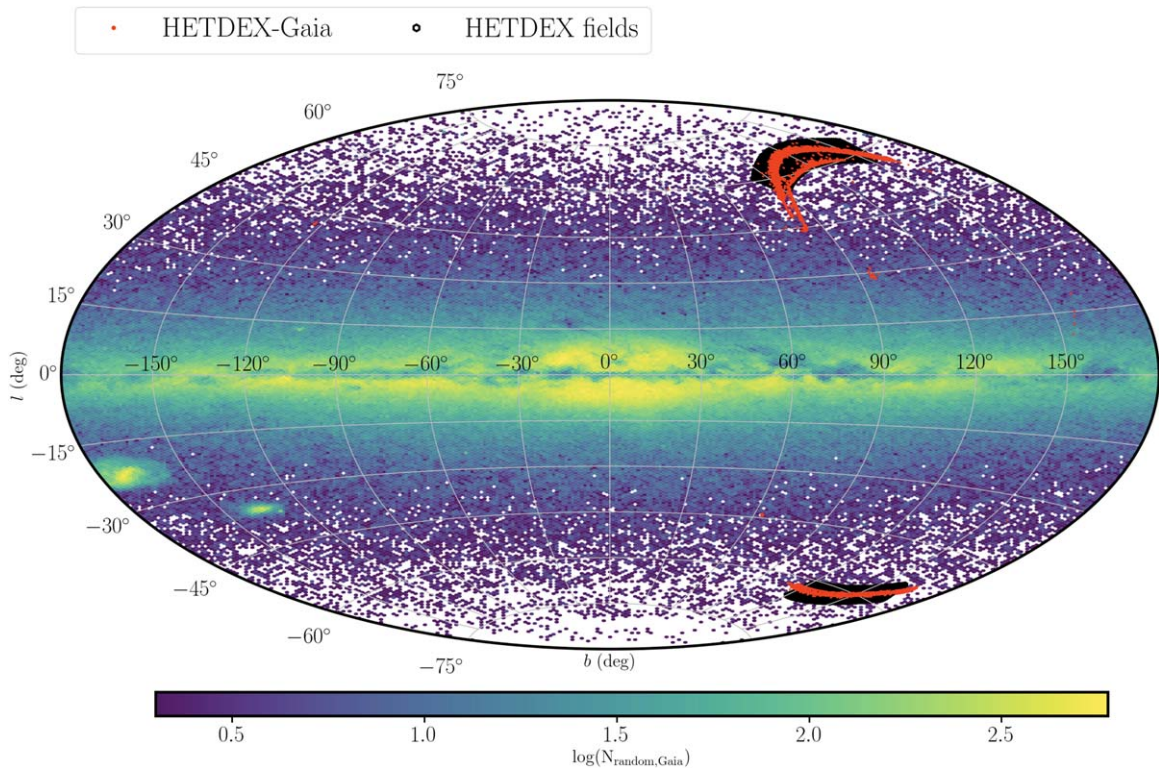


Figure 1. Aitoff projection of the Galactic coordinates for the HETDEX fields (black pentagons) and stars observed in this data release (red circles). For reference, we also show positions for two million randomly selected stars from the Gaia mission. While most of the stars lie in the main HETDEX footprint (at high Galactic latitude), there are some that can also be found in early calibration and extension fields.

comprising ~ 450 sq. deg with a $1/4.5$ fill factor. The current release of HETDEX contains data from ~ 29.85 sq. deg, or $\sim 30\%$ of the expected final HETDEX data set. Figure 1 shows the location of the main HETDEX survey footprint (black) and a density map of two million randomly selected stars from the Gaia mission. The background collection of stars from Gaia is to provide a Galactic context to the HETDEX fields. Also shown are the Galactic coordinates of the stars (Section 2.2) in this data release of the HETDEX survey (red points).

Each HETDEX pointing consists of a set of three-dithered six minute exposures (done in order to fill the sky gaps between fibers; K. Gebhardt et al. 2021, in preparation). The HETDEX fields are mostly at high Galactic latitude, with a median absolute Galactic latitude of $\sim 60^\circ$ (see Figure 1). In HETDEX’s quest to survey $\sim 10^6$ Ly α emitters, it will also capture spectra for many ($\sim 10^5$) stars. It is these stars that are the subject of this work. We make use of the second internal data release for the HETDEX survey, which we will refer to as iHDR2.

2.2. The HETDEX–Gaia Value-added Catalog

The primary goal of this work is to build a catalog of stellar spectra observed within the HETDEX survey and use those spectra to (1) measure RVs for Gaia sources and (2) find metal-poor candidate stars. To achieve these aims we must first obtain a list of point sources (i.e., stars) in the HETDEX survey. This task is accomplished by cross-matching each centroid of each fiber pointing that exists in iHDR2, which includes ~ 200 million spectra, against the ~ 1.7 billion point sources in the Gaia DR2 catalog (Gaia Collaboration et al. 2018). In order to determine the stars in common between HETDEX and Gaia, we cross-match each fiber center in iHDR2 with Gaia

DR2 using a generous $3''$ search radius in R.A. and decl. This relatively large cross-match radius compared to the $1''.5$ fiber diameter of VIRUS ensures that we capture the stars that overlap between HETDEX and Gaia DR2. The result of this cross-match is referred to as the HETDEX–Gaia value-added catalog. We note that distant galaxies can also appear as point sources and therefore we expect some level of contamination from galaxies in our sample.

The final HETDEX–Gaia value-added catalog contains 98,736 unique point sources in the Gaia DR2 catalog with spectral data from HETDEX. Table 1 is subsample of the observational and spectroscopic properties of this catalog. The full catalog will be available online. With the cross-match in hand, we re-extracted the HETDEX spectra at the Gaia DR2 positions accounting for proper motion on the date of the HETDEX observation. If a Gaia DR2 source was observed on multiple nights, multiple independent extractions were performed. We used an optimal method (Horne 1986) for extraction that employs a Moffat spatial profile (Moffat 1969) set to the seeing conditions of the observation as well as a maximum aperture of $3''$.

To perform extractions for any individual source we collect all fibers within $7''$. We use the seeing conditions of the observation to construct a Moffat spatial profile (Moffat 1969) and we integrate that profile over the $1''.5$ diameter fibers. The integral of the profile over the fiber is called the covering fraction. This covering fraction depends on the distance of the source from the fiber center, the seeing conditions, and the wavelength, as the HET does not correct for differential atmospheric refraction so the position of a source with respect to the fiber location changes as a function of wavelength. We illustrate the fiber coverage fractions in Figure 3. We use these

Table 1
The HETDEX–Gaia Value-added Catalog

Gaia Source ID	R.A. (deg)	Decl. (deg)	G (mag)	$BP - RP$ (mag)	S/N_{HETDEX} (pixel^{-1})	RV (km s^{-1})	σRV (km s^{-1})	Barycentric Correction (km s^{-1})	...
2543173457359409664	9.78194	-0.00009	13.06	0.92	58.73	-8.49	28.62	4.18	...
2543068690220755456	10.45149	0.00748	19.15	1.90	3.58	-192.69	62.57	4.19	...
2543068690220758144	10.45224	0.01046	18.88	1.90	5.73	75.98	45.75	4.19	...
2543092398440275072	10.49391	0.05285	20.32	0.81	5.73	-206.13	63.73	4.22	...
2543733211856949120	6.67326	-0.02982	17.51	1.12	29.14	-17.25	19.08	-6.87	...
2543740010789142528	6.84129	0.01837	20.58	1.08	4.21	-55.21	22.88	-6.78	...
2543735509663099648	6.84963	-0.00984	19.52	1.55	7.90	-14.42	35.71	-6.78	...
2543040137278030848	10.73567	-0.04865	17.18	1.85	20.31	-11.99	57.23	-4.99	...
2543039381363775232	10.74644	-0.05880	20.23	1.58	2.64	51.64	50.80	-4.99	...
2543041030631244928	10.79130	-0.03320	19.38	1.74	4.69	-90.57	40.68	-4.96	...
2543041408588483968	10.86433	0.00056	19.81	1.27	5.91	-272.85	137.26	5.40	...
2543175415864489472	9.61114	-0.01187	17.25	1.29	48.19	-471.99	143.30	4.10	...
2543172009953849344	9.62519	-0.04361	19.58	1.08	10.82	-111.52	18.64	4.10	...
2543174728669728768	9.75072	0.05631	19.33	1.33	27.20	2.98	32.01	4.18	...
2543174385072345216	9.77910	0.02872	17.40	1.27	30.14	-56.76	25.57	4.19	...
2543173457359409664	9.78194	-0.00009	13.06	0.92	95.78	28.80	14.25	4.18	...
2543736579111320448	6.96626	0.01918	17.92	1.34	20.29	-17.54	20.59	-7.54	...
2543831343269590656	7.00635	0.06922	12.79	0.89	65.11	-24.53	12.01	-7.51	...
2543547463111076864	7.06080	-0.05459	14.78	0.90	68.92	-70.10	11.09	-7.51	...
2543642295989347840	7.08448	-0.00604	16.59	1.42	35.53	25.00	24.06	-7.49	...
...

Note. This is a subsample of the full HETDEX–Gaia value-added catalog. The Gaia DR2 source identifier of each star is given in column 1 with equatorial coordinates (in J2015.5) in columns 2 and 3. The Gaia G band magnitude and the $BP - RP$ color for each star are listed in columns 4 and 5, respectively. The average S/N per pixel estimated using the HETDEX spectra is given in column 6. The RV and its uncertainty measured from cross-correlating the HETDEX spectra against a template spectrum are listed in columns 7 and 8, respectively. The heliocentric correction, used to correct the measured RV into the rest frame of the Sun, can be found in column 9. This is only a subsample of the full table, which will be provided online, to illustrate the the catalog’s format.

(This table is available in its entirety in machine-readable form.)

fractions as weights in an optimal extraction (Horne 1986). Each extracted spectrum includes the calibrated flux (in units of $\times 10^{-17} \text{ erg cm}^{-2} \text{ s}^{-1}$), a 1σ error array, and a fiber coverage array. The fiber coverage array is defined as the fraction of light that the HETDEX fibers collect for a given point source at a given wavelength. The sky background is estimated using the biweight of all fibers in the observation after the fibers have been flat-fielded using twilight observations. We do not remove contamination from nearby sources. We exclude sources for which fiber coverage arrays contain only pixels with coverages less than 5% (i.e., where $<5\%$ of its light from the star made it into all extracted fibers). Detailed information on the re-extraction methods is included in G. Zeimann et al. (2021, in preparation).

In addition, we computed a “continuum normalized” version of the spectral fluxes, which are normalized using the boosted median continuum (BMC; e.g., Rogers et al. 2010; Hawkins et al. 2014). In this approach, the continuum to be divided is defined as a prescribed percentile of the flux in a predefined window. This is a common approach for low-resolution spectra for which the true continuum is extremely difficult to define due to significant line blending. For the purposes of the HETDEX spectra, we chose a window size of 50 \AA (i.e., 25 pixels) and a percentile of 98%. Additionally, we masked any pixel in the spectra that had low ($<50\%$) fiber coverage (i.e., where less than 50% of the light at a given wavelength from the source falls within the extracted fibers). We filled these masked pixels by interpolating the higher-coverage pixels around the masked value(s).

We determined the S/N for each spectrum by dividing the flux by the flux uncertainty for each pixel and taking the

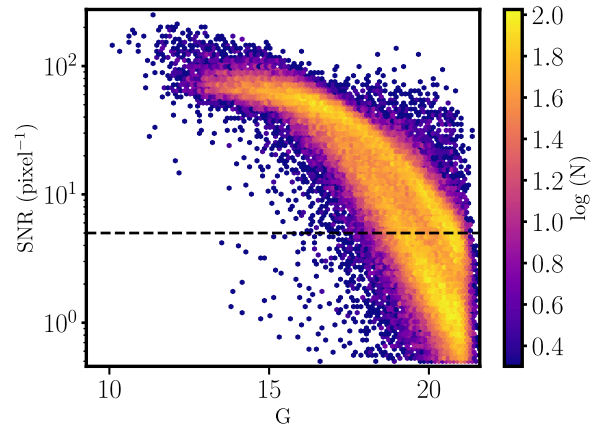


Figure 2. Median S/N per pixel for each star of the 98,736 stars in the HETDEX–Gaia catalog as a function of their Gaia G -band magnitude. The black dashed line represents the $S/N = 5 \text{ pixel}^{-1}$; we generally focus on the $\sim 47,000$ sources above this line.

median over the full spectral range. Figure 2 shows the computed median S/N per pixel for the stars in the HETDEX–Gaia value-added catalog as a function of their G -band magnitude. We generally focus on the 46,890 unique sources with $S/N > 5 \text{ pixel}^{-1}$ in this work. As expected, for a constant exposure time, stars brighter in the Gaia G band have significantly higher S/N . We note that there are likely issues with the brightest stars as they are affected by significant and complex scattered light. HETDEX saturates around $G \sim 14$ mag, and for sources brighter than $G \sim 15$ mag the masking procedures can be aggressive and mistake bright

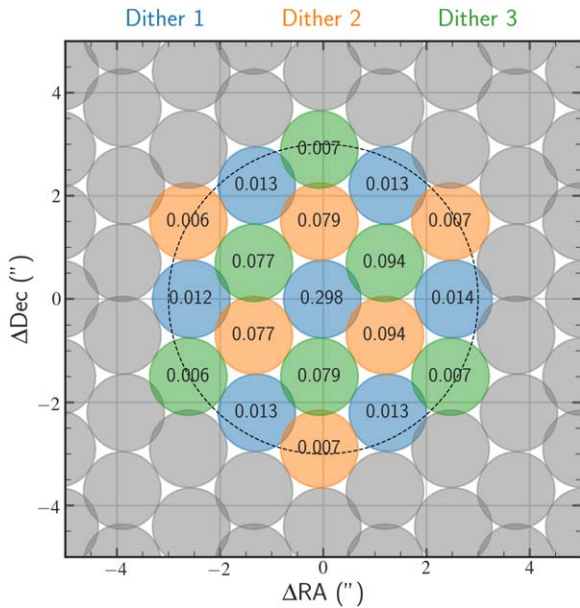


Figure 3. Fiber layout for an example source in an observation with $1''.8$ seeing. The source is at $\Delta R.A. = \Delta \text{decl.} = 0$. A HETDEX observation includes three dithers shown in blue, orange, and green. The fiber diameter is $1''.5$ and in this example, since the closest fiber from dither 1 is nearly centered on the source for extraction, it contains roughly 30% of the total light from the Moffat spatial profile. We show the $3''$ extraction aperture as a dashed black line and the aperture includes all fibers that overlap that radius. We show the fiber coverage for each of the extracted fibers and these coverage values serve as the weights in our optimal extraction. In total 94% of the light is captured in the highlighted fibers. The fibers outside of the extraction aperture are all gray.

spectra for cosmic rays. The observed distribution in parallax (ϖ), G , and $BP - RP$ color for stars with $S/N > 5 \text{ pixel}^{-1}$ can be found in Figure 4. These distributions demonstrate that the most HETDEX stars are farther than 1 kpc, fainter than $G > 18$, and have colors near the turn-off.

To illustrate the stars uncovered in the HETDEX survey as well as their spectral quality, in the left panel of Figure 5 we show the Gaia color–magnitude diagram for those stars of the HETDEX–Gaia value-added catalog with Gaia parallax uncertainty less than 30%. The color used for this work is the difference of the Gaia blue (BP) and red (RP) passbands. For this illustrative plot, we invert the parallaxes to obtain the distance and subsequently the absolute G -band magnitude. However, we note that for larger uncertainties one should not invert the parallax but rather infer the distance given the parallax (e.g., Bailer-Jones 2015; Astraatmadja & Bailer-Jones 2016). We also do not apply reddening corrections to these colors because HETDEX fields were chosen explicitly to have relatively low (i.e., $E(B - V) < 0.05$) extinction. To illustrate the typical HETDEX spectra for different spectral types we median-combine (or stack) stars across 10 absolute magnitude–color bins, which encapsulate the OBAFGKM-type stars (from blue to yellow, respectively) as well as white dwarfs (dark blue), represented by the colors in the left panel of the figure. The spectral stacks contain 100 (white dwarfs) to a few thousand (G -type) spectra. Stars denoted by gray points are those that are not used for the median stack due to low S/N ($S/N < 5$). The right side of Figure 5 shows the median-stacked spectra for white dwarfs to OBAFGKM-type stars from top to bottom. The vertical axis represents the median flux with an additive constant to offset the spectra for the purposes of visualization. Figure 5 shows that HETDEX spectra are of high

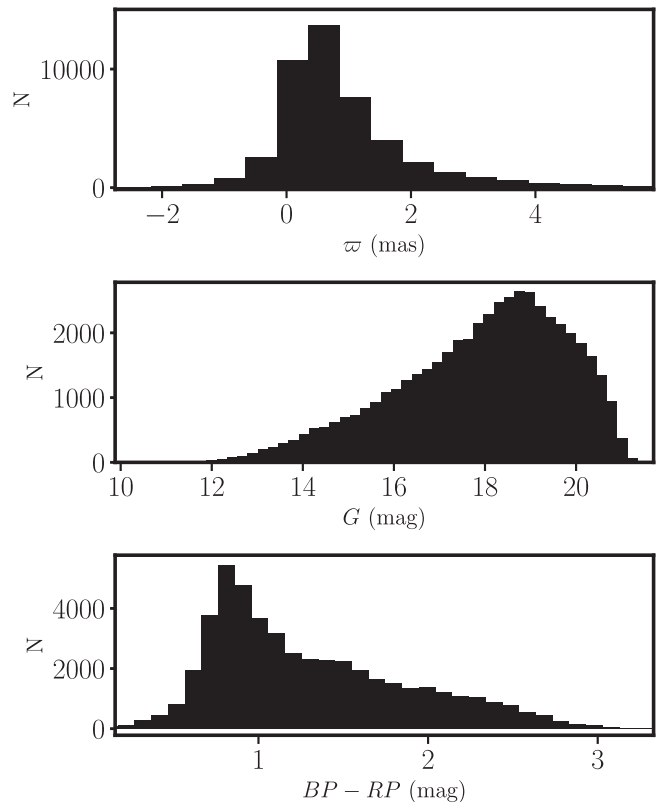


Figure 4. Distribution of parallax (ϖ , top panel), G -band magnitude (middle panel), and $BP - RP$ color (bottom panel) for the stars whose $S/N > 5$.

enough resolution and quality to identify key stellar features (e.g., Ca H&K, CH G -band, $H\beta$, Mg Triplet, TiO molecular band head, etc.).

2.3. Other Large Spectroscopic Surveys: LAMOST and SDSS

To better understand the information content of the HETDEX spectra relative to other large multi-object spectroscopic surveys, we have matched several of these surveys with the HETDEX–Gaia value-added catalog described in Section 2.1. The cross-matches were performed with the fifth data release of the LAMOST survey, the 16th data release of the APOGEE survey, and the ninth data release of the SEGUE survey. These matches were accomplished using a $1''.5$ search window in each of the surveys centered around each point source in the HETDEX–Gaia catalog. We did not cross-match against southern hemisphere spectroscopic surveys (e.g., Gaia-ESO, GALAH, RAVE) because HETDEX was carried out in the northern hemisphere and thus we do not expect many overlapping stars.

The cross-match with the above three surveys have 6364 point sources in common with the LAMOST survey (HETDEX–LAMOST catalog), 5730 point sources in common with the SEGUE survey (HETDEX–SEGUE catalog), and 658 point sources in common with the APOGEE survey. In Table 2, we summarize the depth, resolution, and overlap between the surveys discussed above. It is clear from Table 2 that HETDEX will cover a magnitude space that few stellar spectroscopic surveys cover. Given the low sample size in the cross-match with the APOGEE survey, we will not consider HETDEX–APOGEE cross-matches subsequently in this paper.

For a reliable comparison, we use only a subset of the HETDEX–LAMOST and HETDEX–SEGUE catalogs. For the

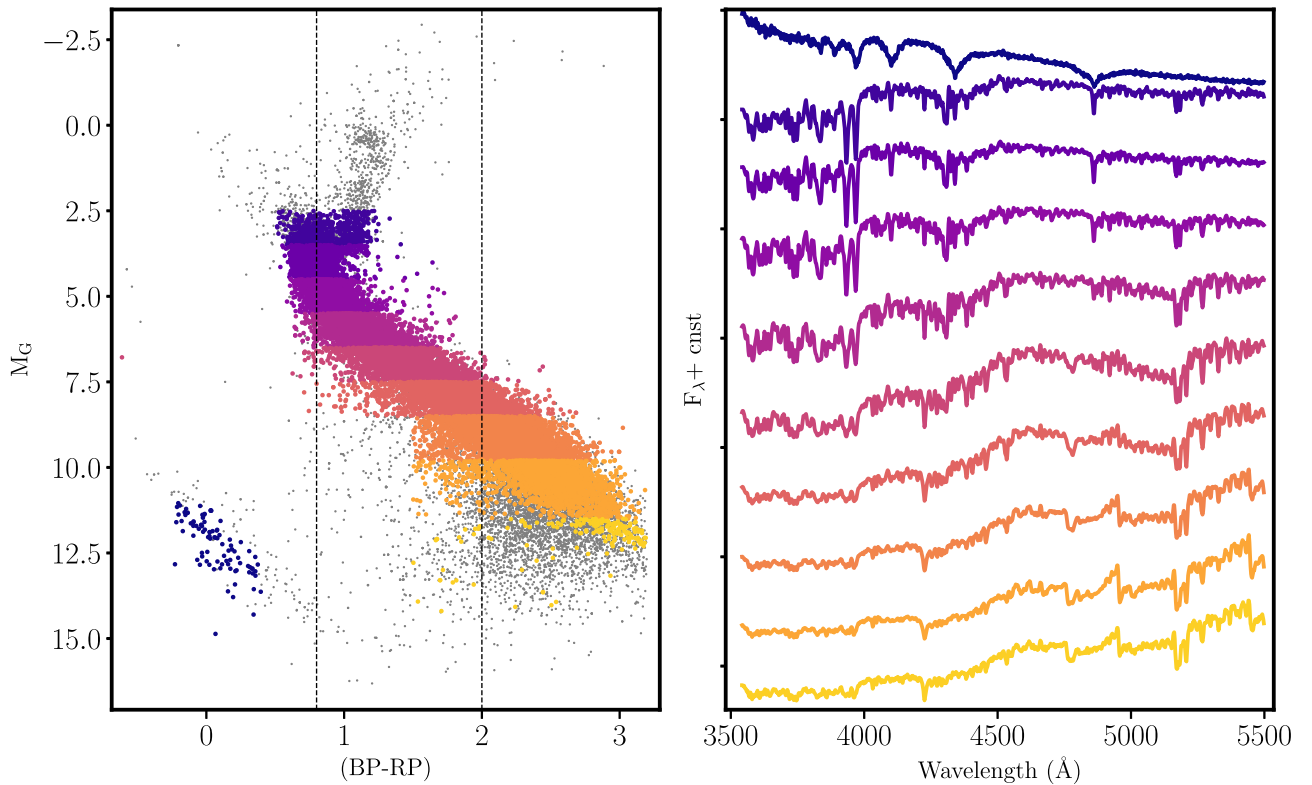


Figure 5. Left panel: color–magnitude diagram of the Gaia–HETDEX value-added catalog for stars for which the parallax uncertainty is less than 30% (gray points). The dotted black lines represent the color range $0.8 < BP - RP < 2.0$, which we focus on in this work. Right panel: median-combined spectra for stars in different regions of the color–magnitude diagram with $S/N > 5$. Spectra are offset by a constant in order to visualize them on the same plot. Each star represented by a colored circle in the left panel was used to generate the median-stacked spectrum (with the same color) in the right panel.

Table 2
Overlap between HETDEX and Other Large Surveys

Survey	\bar{G} (mag)	σG (mag)	Overlap N	Resolution
HETDEX	18.8	2.1	...	750
SEGUE	17.2	1.3	5730	2000
LAMOST	15.1	1.9	6364	1800
APOGEE	13.5	2.1	658	22500

Note. Summary of the overlap between HETDEX and other large spectroscopic surveys. Each survey considered is shown in column 1. The average (\bar{G}) and standard deviation (σG) of the Gaia G band magnitude that the survey covers can be found in column 2 and 3, respectively. The overlap between HETDEX and each survey and its resolution is displayed in columns 4 and 5, respectively.

former, we require the following: (1) the absolute value of the LAMOST RV to be less than 600 km s^{-1} , (2) the uncertainty in RV to be less than 10 km s^{-1} , and (3) the LAMOST S/N in the G band must be larger than 5. The first three constraints were designed to ensure that the LAMOST RV is fairly well determined. Additionally, we require (1) the absolute value of the HETDEX measured RV¹⁵ to be less than 600 km s^{-1} , (2) the uncertainty in the HETDEX RV to be less than 50 km s^{-1} , and (3) the HETDEX S/N to be larger than 5. These last three criteria were required to ensure that reasonable RVs were determined from the HETDEX spectra. For example, when the

¹⁵ There are ~ 600 point sources in the HETDEX–Gaia value-added catalog that have RVs well above 600 km s^{-1} . Visual inspection of the spectra of these sources indicates that they are galaxies.

HETDEX-measured RV uncertainty is larger than 50 km s^{-1} , which happens for a small number of stars in the HETDEX–LAMOST and HETDEX–SEGUE data sets, the RVs are not likely to be reliable. Together these constraints reduced the overall HETDEX–LAMOST catalog to 2384 stars for RV comparisons with a median HETDEX $S/N = 60 \text{ pixel}^{-1}$. We also imposed the same set of quality criteria on the HETDEX–SEGUE catalog, which reduced the comparison sample to 1456 stars, with a median HETDEX $S/N = 30 \text{ pixel}^{-1}$. These comparison samples enable robust quantification of the external precision with which we can estimate RVs using the HETDEX spectra (see Section 4.1).

3. Methods

The primary aims of this paper are to present the first stellar spectra for the HETDEX survey, determine the RVs for the HETDEX–Gaia value-added catalog, and find any candidate metal-poor stars hidden within the low-resolution data. As such, in the following sections, we outline the methods used to measure the RVs from HETDEX spectra (Section 3.1) and identify potential metal-poor candidate stars (Section 3.2).

3.1. Radial Velocities

The RVs for HETDEX spectra are determined using the cross-correlation technique, whereby the observed spectrum is compared to a template spectrum. To do this, we made use of the *iSpec* python package (Blanco-Cuaresma et al. 2014). *iSpec* cross-correlates the observed spectra with a template spectrum within a specific velocity range and step. A grid of RV template spectra was generated using the TURBOSPECTRUM

(Alvarez & Plez 1998; Plez 2012) radiative transfer package along with the MARCS model atmosphere grid (Gustafsson et al. 2008) and version 5 of the Gaia-ESO linelist. The same spectral synthesis configuration is also used in Hawkins et al. (2020), although here it is at much lower spectral resolution. These template spectra were generated with a wavelength coverage of $3500 < \lambda < 5500 \text{ \AA}$ and a resolution of $R = 750$ to approximately match the HETDEX spectra. The grid was generated for temperatures between $4000 < T_{\text{eff}} < 7000 \text{ K}$ in steps of 250 K, log gravities from $0.5 < \log g < 5.0 \text{ dex}$ in steps of 0.5 dex, and metallicities between $-2.0 < [\text{Fe}/\text{H}] < +0.5 \text{ dex}$ in steps of 0.50 dex. Given the temperature range of the grid, we restrict our further analysis to stars with $0.8 < (BP - RP) < 2.0$.

Once the RV template grid was constructed, each HETDEX spectrum was matched to one of the template spectra by minimizing the χ^2 . The template spectral grid was also normalized using the BMC to be consistent with the observed spectra. The cross-correlation was done in velocity space with RVs between $-1000 < \text{RV} < +1000 \text{ km s}^{-1}$ and a velocity step of 1 km s^{-1} . `iSpec`¹⁶ determines the RV by fitting a second-order polynomial near the peak of the cross-correlation function, and indicates if there are multiple peaks in the cross-correlation, which could represent the presence of a binary companion. After the RVs are determined for each star, the barycentric correction using `iSpec` is applied to the RV. As noted in the `iSpec` documentation, the uncertainties in the RV are determined using the cross-correlation function and its second derivative according to Zucker (2003).

3.2. Categorizing the HETDEX Stars Using Machine Learning: tSNE

In addition to measuring the RVs for HETDEX stellar spectra, we are also interested in identifying any metal-poor stars in these low-resolution data, as this has not yet been done for this data set. One way of categorizing stars on the basis of how similar their spectra appear is through tSNE (van der Maaten & Hinton 2008). tSNE is a machine-learning technique that enables the construction of a low, normally two-dimensional (2D), projection of a higher-dimensional data set while efficiently retaining much of its original complexity. tSNE has been used by several other surveys to characterize their stellar spectra. For example, it has been employed by Matijević et al. (2017) to find very metal-poor stars in the RAVE survey, by Anders et al. (2018) to explore the practicality for chemical tagging purposes with high-resolution data taken with the HARPS spectrograph, and by Jofré et al. (2017) to search for stellar twins. For the purposes of our work here, we use tSNE to explore whether the HETDEX spectra are of sufficient quality to find metal-poor stars, similar to Matijević et al. (2017), but at the lowest resolution to date and applied for the first time to this data set. In the context of HETDEX spectra, tSNE will enable representation of all of the $D = 1036$ pixel, RV-corrected, low-resolution HETDEX spectra on a 2D plane where stars with similar spectra are found in the same region of that space, and stars that have very dissimilar spectra are separated in that space.

While a detailed description and discussion of tSNE can be found in van der Maaten & Hinton (2008), we summarize the technique and how we apply it to the HETDEX spectra in this work. In order for tSNE to capture the complexity of the original high-D data set, which in the context of HETDEX is the matrix

of flux densities that describe all of the spectra, it must first determine the similarity between each data spectrum and all others. In this paper, we define the set of fluxes that describe a star’s spectrum as $\mathbf{f} = \{f_i\}$ where $\{f_i\}$ is the array of fluxes at a given set of i th wavelengths. The bolded symbols denote vectors. Additionally, the matrix of fluxes across all RV-corrected, BMC-normalized HETDEX spectra input into tSNE is defined as $\mathbf{F} = \{\mathbf{f}_k\}$ where \mathbf{f}_k represents the k th spectrum in the data set. Throughout the text, bold upper-case symbols represent matrices. Each row of the matrix \mathbf{F} is an individual spectrum/star and can be thought of as a single data point in the high-D data set that tSNE will project onto a 2D plane.

To describe the similarity of each spectrum against all other spectra, tSNE starts by representing each “point” (i.e., a HETDEX spectrum) in the high-D space as a Gaussian probability distribution. That Gaussian distribution is centered on each “point” with a dispersion of σ_i . The σ_i is not the uncertainty in the data point but rather set by a parameter called *perplexity*. As noted in van der Maaten & Hinton (2008), the perplexity is tied to the effective number of neighbors expected in the data set. Once tSNE represents the similarity of each spectrum against all other spectra, it will “embed” that similarity of each star with all other remaining stars in the high-D data set through the conditional probability, $p_{j|i}$, such that

$$p_{j|i} = \frac{\exp(-\|\mathbf{f}_i - \mathbf{f}_j\|^2 / 2\sigma_i^2)}{\sum_{k \neq i} \exp(-\|\mathbf{f}_i - \mathbf{f}_k\|^2 / 2\sigma_i^2)}. \quad (1)$$

In Equation (1), $p_{j|i}$ is the conditional probability that the j th spectrum (\mathbf{f}_j) would select the i th the spectrum (\mathbf{f}_i) as its neighbor, and thus formalizes the similarity between these two spectra. The higher this conditional probability, the more similar the data points are and vice versa. Since tSNE focuses on pairwise similarities, $p_{j|i}$ is set to 0. As described in van der Maaten & Hinton (2008), it is not expected that the performance of tSNE will be significantly affected by changes of perplexity between 5 and 50. We also confirmed that the global shape of the tSNE map of our data does not change with perplexity between these values.

Encoded in $p_{j|i}$ (Equation (1)) is the similarity of each spectrum against all other spectra in the data set. The next step is to embed this complex information onto a 2D plane while minimizing the loss of information. To accomplish this, each data point in the high-D space (i.e., each HETDEX spectrum) is projected onto a 2D plane, where the i th spectrum in this low-D space is given by the quantity \mathbf{y}_i . As in the high-D case above, the similarity of each spectral projection in 2D against all others can be formalized as a conditional probability, $q_{j|i}$, such that

$$q_{j|i} = \frac{(1 + \|\mathbf{y}_i - \mathbf{y}_j\|^2)^{-1}}{\sum_{k \neq i} (1 + \|\mathbf{y}_i - \mathbf{y}_k\|^2)^{-1}}. \quad (2)$$

In Equation (2), the similarities between the 2D spectral projection of the j th (\mathbf{y}_j) and the i th (\mathbf{y}_i) data points are modeled not as a Gaussian distribution but as a Student t-distribution with a single degree of freedom. We refer the reader to van der Maaten & Hinton (2008) for a detailed discussion as to why the t-distribution is conveniently chosen over a Gaussian distribution as in Equation (1).

The final step of tSNE is to find a projection in the 2D space such that $q_{j|i} = p_{j|i}$, as it is in this case that the \mathbf{y}_j and \mathbf{y}_i are correct models of their higher-D equivalents (\mathbf{f}_j , \mathbf{f}_i).

¹⁶ For more information see Blanco-Cuaresma et al. (2014) and <https://www.blancocuaresma.com/s/iSpec/manual/usage/velocities>.

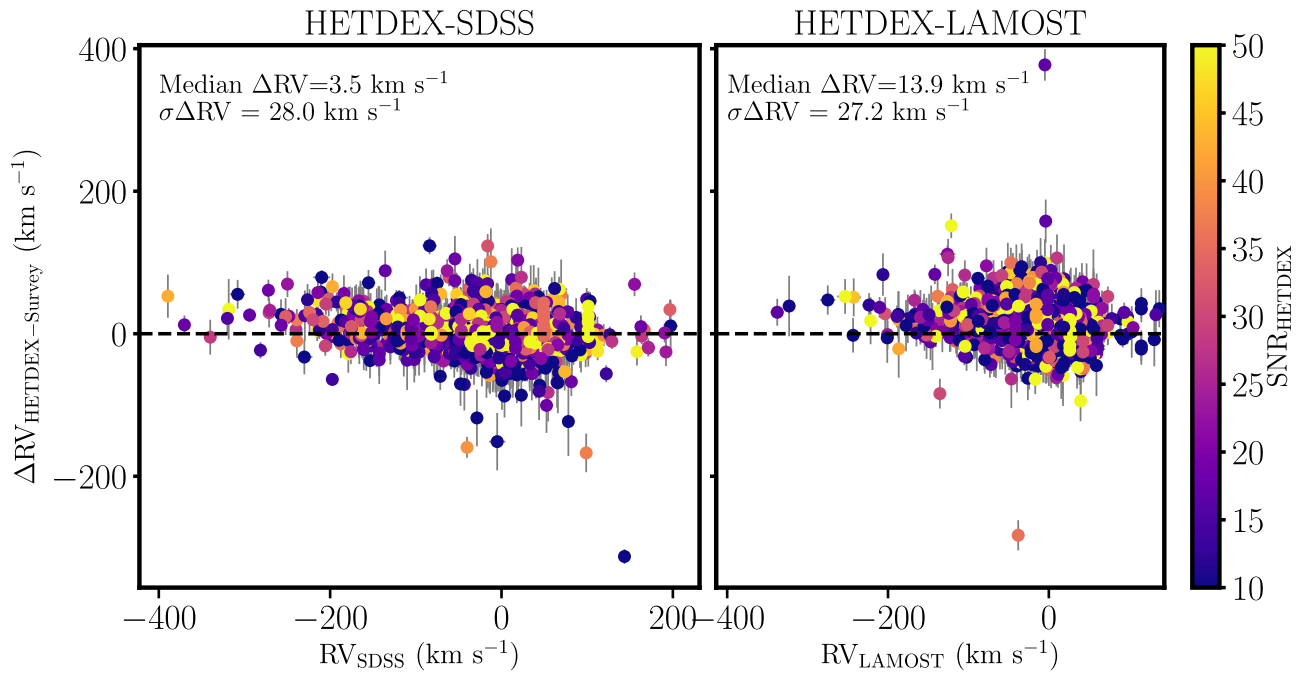


Figure 6. Difference RV determined using HETDEX spectra and those from SEGUE as a function of the SEGUE RV (left panel). The same is shown on the right panel but for the LAMOST survey. Each star is color-coded by its S/N. The dotted black line in both represents when the HETDEX-measured RV directly matches that measured by the external survey. The median offset and dispersion of the difference in RV, ΔRV , are noted in the diagram.

Unfortunately, this idealized condition never occurs in practice so the approach of tSNE is to make $q_{ji} \approx p_{ji}$ by minimizing the Kullback–Leibler divergence (KLD, Kullback 1959), over all points. This KLD cost function is given by

$$C = \sum_i \sum_j p_{ji} \log \frac{p_{ji}}{q_{ji}}. \quad (3)$$

In Equation (3), the parameter C is the KLD cost function to be minimized, while q_{ji} (Equation (2)) and p_{ji} (Equation (1)) are the conditional probabilities that describe the similarity between the j th and i th points in the low-D and high-D spaces, respectively.

We made use of an accelerated version of tSNE¹⁷ (van der Maaten 2014), which employs the Barnes–Hut algorithm (Barnes & Hut 1986). This implementation of tSNE has two tunable hyperparameters, which are the perplexity, discussed above, and θ , which ranges from 0 to 1 and sets the speed-to-accuracy of the algorithm. If θ is set to 1 the algorithm can run very fast (\sim a few seconds) but with less accuracy. However, if θ is set to 0, high accuracy can be achieved but at the cost of computation time. Here we choose $\theta = 0.1$ and perplexity = 20 because our sample size is not significantly large compared to sample sizes usually input to tSNE. The algorithm required ~ 600 s to run on a single computer core for the full sample under these conditions.

4. Results and Discussion: Exploring the Stars of the HETDEX Survey

4.1. Radial Velocities

Our first goal was to measure HETDEX spectra RVs for stars with colors between $0.8 < (BP - RP) < 2.0$. The RVs were determined using the cross-correlation technique with a spectrum chosen from a grid of template spectra by identifying

the best-fitting synthetic spectrum. We refer the reader to Section 3.1 for more details about the construction of the template grid, how the templates are matched to the observed spectra, and how the RVs were determined. The color range was selected in order to ensure that the T_{eff} of the star was not significantly hotter or cooler than the boundaries of the RV template grid. We were able to derive RVs, their uncertainties, and heliocentric corrections for 41,980 unique stars. However, many of these spectra have $S/N < 5 \text{ pixel}^{-1}$ and are therefore unlikely to yield high-quality RV estimates. If we restrict our analysis to only those spectra with $S/N > 5 \text{ pixel}^{-1}$, we obtain 28,343 stars. Of these 28,343 stars, ~ 602 ($\sim 2\%$) have RVs larger than 600 km s^{-1} . Visual inspection of the HETDEX spectra of these objects indicate that they are likely to be galaxies, so we remove any source with a measured RV larger than 600 km s^{-1} from our sample.

In order to validate the quality of the RVs determined from the HETDEX spectra (described in Section 2.2) and the cross-correlation technique (outlined in Section 3.1), we cross-matched these stars against other large spectroscopic surveys at higher resolution (i.e., SEGUE and LAMOST). For the HETDEX–SEGUE cross-match, which initially contained about 5700 stars, we required that the SEGUE RV must be known with an uncertainty of less than 10 km s^{-1} and a SEGUE-derived $S/N > 10$. We also required the HETDEX-derived RV to be less than 600 km s^{-1} . These constrained reduced the HETDEX–SEGUE comparison to 1456 stars. For the HETDEX–LAMOST comparison, which initially contained around 6300 stars, we applied the same criteria as for the HETDEX–SEGUE comparison, which reduced the HETDEX–LAMOST external validation sample to 2384 stars (see Section 2.3 for more details).

Figure 6 presents the HETDEX RVs measured in this work compared with those measured for the same stars in the HETDEX–SEGUE (left panel) and the HETDEX–LAMOST (right panel) comparison samples. Each point represents an

¹⁷ The python implementation of tSNE we employed can be found at <https://github.com/lvdmaaten/bhtsne/>.

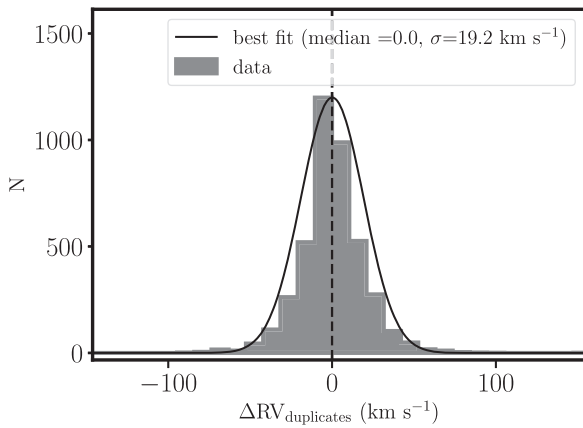


Figure 7. Distribution of the $\Delta RV_{\text{duplicates}}$ for the ~ 2000 stars with more than one epoch of spectra from HETDEX. The quantity $\Delta RV_{\text{duplicates}}$ is the RV measured in all epoch subtracted from the median RV across all epochs for each star. The offset is consistent with zero while the dispersion, which is a measure of the internal precision, is $\sim 19 \text{ km s}^{-1}$ (black line).

individual star and the points are color-coded by the HETDEX S/N. Figure 6 indicates that there is generally good agreement between the RVs measured by HETDEX and those by SEGUE with a systematic offset of $+3.5 \text{ km s}^{-1}$ and a dispersion in the difference in RV, ΔRV , of 28.0 km s^{-1} (i.e., the RV measured by HETDEX is 3.5 km s^{-1} larger than those from SEGUE). There is fair agreement between the RVs measured by HETDEX and those by LAMOST with a systematic offset of $+13.9 \text{ km s}^{-1}$ and a dispersion in the ΔRV of 27.2 km s^{-1} (i.e., the RV measured by HETDEX is 13.9 km s^{-1} larger than those from LAMOST). Additionally, there is a known difference of $\sim +9.1 \text{ km s}^{-1}$ difference in the RVs measured by LAMOST compared to those by SEGUE (whereby the SEGUE RVs are 9.1 km s^{-1} larger than those from LAMOST) for the 66 stars that are in common between all three surveys and pass all quality criteria,¹⁸ indicating that the differences in the RV offset that we observe between the HETDEX–LAMOST ($+13.9 \text{ km s}^{-1}$) and HETDEX–SEGUE (3.5 km s^{-1}) validation sets can be fully accounted for by the difference in the two RV scales. There is good agreement in the external precision (measured to be $\sim 28 \text{ km s}^{-1}$), to which we can measure RVs relative to the two independent validation sets. We note that these results are not significantly dependent on the median fraction of flux coverage of individual sources across fibers.

We can further test the measured RV precision in the HETDEX survey by quantifying the internal precision, i.e., by determining how consistent the HETDEX RVs are between stars with spectra obtained from multiple epochs. There are ~ 2000 unique stars that have multiple epochs of measured RVs. For each unique star with multiple spectra (and therefore multiple RV estimates), we obtain the difference in RV in each epoch and the median RV across all visits. We denote this quantity as $\Delta RV_{\text{duplicates}}$. The distribution of $\Delta RV_{\text{duplicates}}$ can be found in Figure 7. There is an offset consistent with zero and a dispersion in $\Delta RV_{\text{duplicates}}$ is 19.1 km s^{-1} . The dispersion in $\Delta RV_{\text{duplicates}}$ represents a measure of the internal precision with which we can measure RVs from duplicate observations of the same (assumed to be single) stars.

¹⁸ This is consistent with the observed offset between the full cross match of the LAMOST and SEGUE surveys; for example see Section 3 of <http://dr5.lamost.org/v3/doc/release-note-v3>.

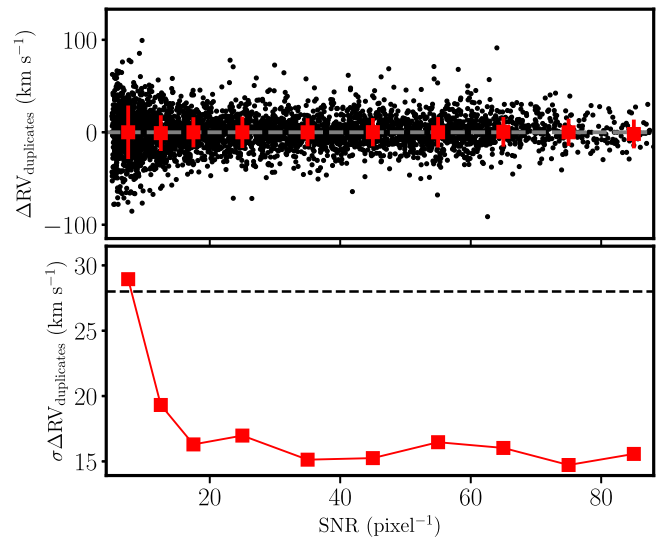


Figure 8. Top panel: difference in the RVs measured between epochs and the median RV, $\Delta RV_{\text{duplicates}}$, for each star that has duplicate spectra as a function of the HETDEX S/N. The red squares represent the median and dispersion of $\Delta RV_{\text{duplicates}}$ in 10 S/N bins. Bottom panel: dispersion in $\Delta RV_{\text{duplicates}}$, a measure of the internal RV precision, as a function of HETDEX S/N. The dispersion in $\Delta RV_{\text{duplicates}}$ is $\sim 15 \text{ km s}^{-1}$ for the highest S/N (S/N $> 30 \text{ pixel}^{-1}$), and rises to $\sim 29 \text{ km s}^{-1}$ for the lowest S/N (S/N $\sim 5 \text{ pixel}^{-1}$).

Figure 8 shows how the internal precision, as measured by the dispersion in $\Delta RV_{\text{duplicates}}$, depends on S/N. As expected, the internal precision of RV measurements from HETDEX spectra degrades with decreasing S/N. The highest precision is for stars with S/N $> 30 \text{ pixel}^{-1}$ and the lowest is for those with S/N $< 10 \text{ pixel}^{-1}$. In the S/N regime that dominates the external validation sets, the internal (as measured by the duplicate spectra) and external precisions (as measured by the validation sets) are consistent. We assume that each star in the above analysis is a single star. If there were a significant fraction of unknown binaries, it would cause some of the scatter in the $\Delta RV_{\text{duplicates}}$.

Taken together, these results indicate that we can conservatively measure RVs in HETDEX at the $\sim 28 \text{ km s}^{-1}$ level. We also find that the RVs measured with the HETDEX spectra most closely resemble those from SEGUE. However, SEGUE has an empirical correction on the order of $\sim 8 \text{ km s}^{-1}$ with respect to published values from star clusters (e.g., Lee et al. 2008a). Additionally, since RVs measured with LAMOST have a much lower zero-point correction (e.g., 0.02 km s^{-1} ; Wang et al. 2019), we recommend subtracting 13.5 km s^{-1} from the reported RVs to bring them onto the LAMOST RV scale.

With the RVs in hand, we correct all spectra to be in the rest frame and move on to exploring the information content of the spectra through machine learning.

4.2. Finding Metal-poor Stars in HETDEX with Machine Learning

Using the RV-corrected HETDEX spectra, we are able to potentially identify new metal-poor stars. To achieve this, we adopt the machine-learning tSNE (Section 3.2) with the HETDEX spectroscopic data. We input into tSNE the BMC-normalized (see Section 2.2), RV-corrected (see Sections 3.1

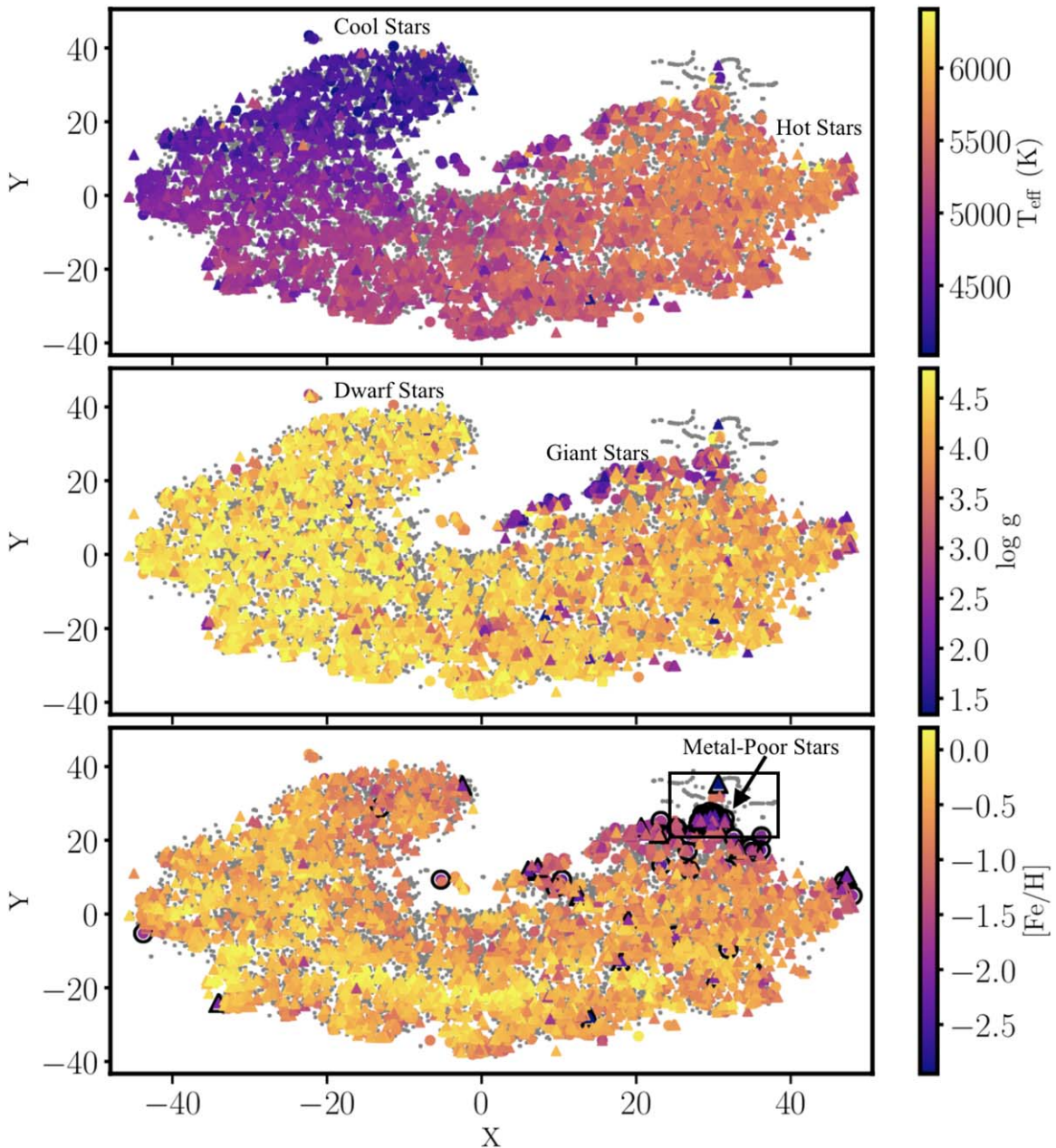


Figure 9. Two-dimensional tSNE maps (in X and Y) of the HETDEX sample with RV measurements (small gray points). We highlight, by color-coding, any star with a known T_{eff} (top panel), $\log g$ (middle panel), or $[\text{Fe}/\text{H}]$ (bottom panel) from the SEGUE (colored circles) and LAMOST (colored triangles) surveys. In the bottom panel, metal-poor stars, with $[\text{Fe}/\text{H}] < -1.8$ dex, are highlighted with a black border around the symbol.

and 4.1) spectra for stars with $0.8 < (BP - RP) < 2.0$ ¹⁹. The tSNE algorithm requires all spectra to be sampled on the same wavelength grid with no missing pixels (due to low coverage fractions, for example). To construct this data set, we resampled the HETDEX spectra onto the same wavelength grid between $3640 < \lambda < 5340 \text{ \AA}$ with 2 \AA steps. Since we initially removed fluxes where the coverage fraction is less than 0.50 (see Section 2.2), we interpolated over the removed pixels during the resampling. To minimize the impact of this

¹⁹ In principle, we could input all of the stars in the HETDEX-Gaia value-added catalog into the tSNE algorithm. This would enable us to classify each of the various types from white dwarfs to late-type stars. While we confirmed that tSNE can classify stars outside of the late-type star regime, we focused here on the FGK stars for this first paper and leave it to upcoming papers to discuss chemically peculiar stars found using this methodology.

interpolation, we restricted ourselves to the $\sim 14,000$ stars that have less than 5 pixels where the coverage fraction is less than 0.50 (i.e., we only replaced as many as 5 pixels via interpolation). We initially configured tSNE with perplexity of 20 and a $\theta = 0.10$ with 1000 maximum iterations. We examined both 2D and 3D projections of the data set and found little benefit to higher-D projection.

Figure 9 shows the final projection of the high-D spectral data set in 2D. Each spectrum input into tSNE is represented by a closed gray circle in the figure; the final projection is color-coded by T_{eff} (top panel), $\log g$ (middle panel), and $[\text{Fe}/\text{H}]$ (bottom panel) where those quantities are known by either SEGUE (colored circles) or LAMOST (colored triangles). This color-coding highlighted in this figure illustrates how the tSNE map can be used to identify regions where the spectra are

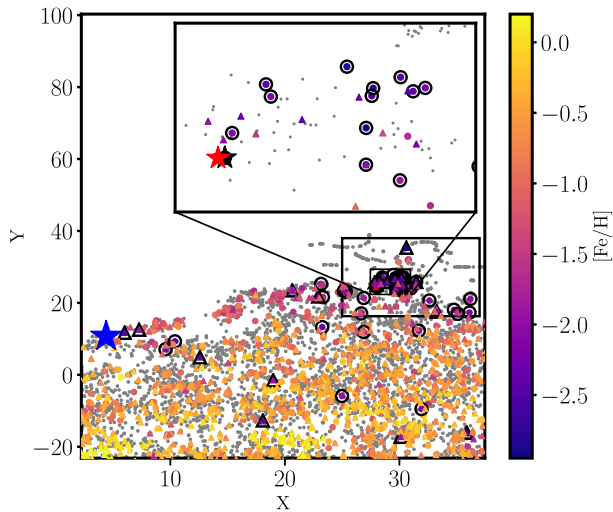


Figure 10. Zoom-in on the bottom panel of Figure 9 inside the metal-poor selection box. The inset is a further expanded view. The red star symbol is a candidate metal-poor star (Gaia DR2 1593425105811347328), which has no known metallicity from any spectroscopic survey to date. The black star symbol is a known metal-poor star (Gaia DR2 2537923358055035648) from SEGUE. For comparison, the blue star symbol is a known more metal-rich star (Gaia DR2 2536562574976818816) with comparable T_{eff} and $\log g$ values. The black star is almost entirely behind the red star because they were selected to be direct neighbors. Nearly all stars in the region with known metallicity have $[\text{Fe}/\text{H}] < -1.0$ dex.

similar (i.e., regions where the stars have similar atmospheric parameters). For example, in the final tSNE diagram, the coolest stars are in the upper corner left of center (i.e., $X \sim -10$, $Y \sim +30$) of the map (see the top panel of Figure 9), the central part of the tSNE map contains the majority of the spectra, and the outer edges contain more peculiar classes of stars. Critically, the bottom panel of Figure 9 demonstrates that the metal-poor stars largely clump up in the top right (i.e., $X \sim 25$, $Y \sim 30$) of the manifold, albeit with some spread. To help guide the eye, we place a black outline around any symbol with $[\text{Fe}/\text{H}] < -1.80$ dex. We also select a region where there is a high density of metal-poor stars (i.e., those with $[\text{Fe}/\text{H}] < -1.0$ dex). This region contains 416 candidate metal-poor stars for further investigation.

Similar to Matijević et al. (2017), Figure 9 demonstrates that it is possible to use HETDEX spectra to identify stars with $[\text{Fe}/\text{H}] < -1.0$ dex. To further illustrate this feature, in Figure 10 we select a known metal-poor star (Gaia DR2 2537923358055035648, black star symbol), which has a published metallicity of $[\text{Fe}/\text{H}] = -2.00$ dex from the SEGUE Stellar Parameter Pipeline (SSPP; Allende Prieto et al. 2008; Lee et al. 2008a, 2008b; Smolinski et al. 2011). This figure is identical to the bottom panel of Figure 9; however, we have enlarged the metal-poor selection box region. We also choose the closest point in tSNE space that does not have a known metallicity (Gaia DR2 1593425105811347328, red star symbol). The red and black stars representing the candidate and known metal-poor stars largely lie on top of each other in Figure 10. Since this star is closest to known metal-poor stars in tSNE space, it is expected that its metallicity is an excellent metal-poor candidate. For reference, the location of a known metal-rich star (Gaia DR2 236562574976818816), with $[\text{Fe}/\text{H}] = -0.34$ dex, is also shown (blue star). This star was selected such that its SSPP T_{eff} was within ± 200 K and its SSPP $\log g$ was within ± 0.20 dex of the known metal-poor star.

Figure 11 displays the RV-corrected, BMC-continuum-normalized HETDEX spectrum of the known metal-poor star (black line), the metal-poor candidate star (red line), and the metal-rich comparison star (blue line). Figure 11 shows that the metal-poor candidate has absorption features that are much weaker than those of the known metal-rich star, and closely resemble those of the metal-poor candidate star. This indicates that the HETDEX spectra are of sufficient quality to find new metal-poor stars. The performance of tSNE is likely driven by the fact that T_{eff} , $[\text{Fe}/\text{H}]$ and, to a lesser degree, $\log g$ information are embedded in the spectra. This could be due to the advantageous wavelength regime, which includes various stellar parameter-sensitive features (e.g., Ca H&K, Balmer lines).

We are currently obtaining observations of the brightest of these metal-poor candidate stars with higher resolution to accurately determine their metallicities and chemical abundances. The candidate metal-poor stars discussed here represent $\sim 3\%$ of the total number of stars input into tSNE. Assuming the same percentage of metal-poor stars but an increase in sample size by $\sim 70\%$, one would naively predict HETDEX to contain thousands of metal-poor stars over its competition. Importantly, since there is no preselection to objects observed in HETDEX, the final metal-poor sample from HETDEX will enable us explore the stellar halo of the Milky Way with a relatively simple and quantifiable selection function.

5. Summary

HETDEX is an ongoing blind spectroscopic survey of more than one million Ly α -emitting galaxies. However, in its search for these galaxies, it will observe 10^5 stars. In this work, we focus on building the first catalog of these stars and illustrate what can be done with them. We found stars in the HETDEX survey by cross-matching more than ~ 200 million HETDEX fiber spectra with the ~ 1.6 billion Gaia point sources. This enabled us find 98,736 unique stars with HETDEX spectra. The spectra cover a broad range in the relatively faint magnitude regime of $10 < G < 21$ mag. Since HETDEX is a blind survey,²⁰ it captures a wide range in stellar types from thousands of M-dwarfs to hundreds of white dwarfs (see Figure 5). For the purposes of this work, we focused our attention on the late-type (largely FGK-type) stars by imposing a color cut of $0.8 < (BP - RP) < 2.0$. RVs were determined for these stars using cross-correlation with template spectra (Section 3.1). The results of that analysis show that RVs derived with HETDEX spectra are in good agreement with those measured by the SEGUE and LAMOST surveys. We find a median offset of 3.5 and 13.9 km s^{-1} with the SEGUE and LAMOST surveys, respectively. Additionally, we demonstrate that the dispersion in the ΔRV between HETDEX and these surveys is $\sim 30 \text{ km s}^{-1}$ (Figures 6 and 7). Since Gaia will only be able to derive RVs for the brightest stars ($G < 14$), for many of the faint stars in HETDEX these results will be their only RV measurement.

We also attempted to determine whether the information content of the low-resolution spectra was enough to find metal-

²⁰ While the HETDEX survey design itself has no target selection, there are several factors (e.g., magnitude limits of the survey, spectral noise, or nearby source contamination) that may imprint biases on the underlying distribution of observed stars. Unlike for most surveys, which suffer major biases due to target selection, the stars of HETDEX will have a relatively simple and quantifiable selection function.

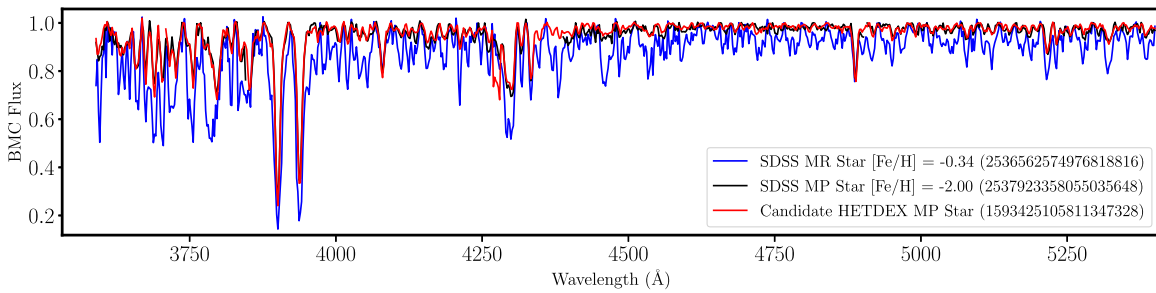


Figure 11. HETDEX spectrum of a candidate metal-poor star (red line) identified from the tSNE map in Figure 9. For reference, also shown as a black line is a known metal-poor ($[\text{Fe}/\text{H}] = -2.00$) star from SEGUE that was closest to the candidate star in the tSNE diagram and a more metal-rich star (blue line), with $[\text{Fe}/\text{H}] = -0.34$ dex, a temperature within ± 200 K in T_{eff} , and $\log g$ within ± 0.20 dex of the known metal-poor star.

poor stars. To do this, we employed the tSNE machine-learning algorithm which projects a high-dimensional data set (i.e., the HETDEX spectra) onto a low-dimensional manifold as a way to visualize the complexity of the data. This method has been employed in recent literature to search for metal-poor stars in moderate-resolution surveys (e.g., Matijević et al. 2017), though here we apply it at the lowest spectral resolution to date. The results of the tSNE analysis can be found in Section 4.2. Using tSNE, we uncovered 416 new metal-poor candidate stars (Figures 9–11), for which higher-resolution spectroscopic followup is underway. The metal-poor stars identified here will be useful in constraining the formation of elements on the periodic table as well the early history of the Milky Way. Additionally, these results indicate that there is enough information embedded in the HETDEX spectra to not only derive T_{eff} , and $\log g$, but $[\text{Fe}/\text{H}]$ as well.

This work represents the first attempt to extract and explore the stars observed by the HETDEX survey. The survey is ongoing and only $\sim 30\%$ complete. Thus it is expected that there will be many more stars in the final HETDEX sample. In an upcoming paper, we plan to validate and chemically characterize the metal-poor candidate stars discovered here with higher-resolution data, use tSNE to find other types of chemically peculiar stars (e.g., carbon-enhanced stars), and attempt to measure the stellar atmospheric parameters directly from HETDEX spectra as we now know the information content is there (e.g., see Figure 9). Additionally, the results presented here provide an example of how low-resolution stellar spectra can be utilized in future surveys (e.g., in the upcoming Nancy Grace Roman Telescope; Green et al. 2012). That combined with the blind nature of the survey will enable future stellar surveys with HETDEX to make a significant impact on Galactic archaeology.

K.H. has been partially supported by a TDA/Scialog (2018–2020) grant funded by the Research Corporation and a TDA/Scialog grant (2019–2021) funded by the Heising-Simons Foundation. K.H. acknowledges support from the National Science Foundation grant AST-1907417 and from the Wootton Center for Astrophysical Plasma Properties funded under the United States Department of Energy collaborative agreement DE-NA0003843. E.S. gratefully acknowledge funding by the Emmy Noether program from the Deutsche Forschungsgemeinschaft (DFG).

The observations were obtained with the Hobby–Eberly Telescope, operated by McDonald Observatory on behalf of the University of Texas at Austin, Pennsylvania State University, Ludwig-Maximilians-Universität München, and Georg-August-Universität, Göttingen. The HET is named in honor

of its principal benefactors, William P. Hobby and Robert E. Eberly. We thank the staff at McDonald Observatory for making this project possible.

HETDEX (including the WFU of the HET) is led by the University of Texas at Austin McDonald Observatory and Department of Astronomy with participation from the Ludwig-Maximilians-Universität München, Max-Planck-Institut für Extraterrestrische-Physik (MPE), Leibniz-Institut für Astrophysik Potsdam (AIP), Texas A&M University, Pennsylvania State University, Institut für Astrophysik Göttingen, The University of Oxford, Max-Planck-Institut für Astrophysik (MPA), The University of Tokyo, and Missouri University of Science and Technology. In addition to Institutional support, HETDEX is funded by the National Science Foundation (grant AST-0926815), the State of Texas, the US Air Force (AFRL FA9451-04-2-0355), and generous support from private individuals and foundations.

The authors acknowledge the Texas Advanced Computing Center (TACC) at The University of Texas at Austin for providing computing resources that have contributed to the research results reported within this paper. URL: <http://www.tacc.utexas.edu>

Funding for the Sloan Digital Sky Survey IV has been provided by the Alfred P. Sloan Foundation, the U.S. Department of Energy Office of Science, and the Participating Institutions. SDSS-IV acknowledges support and resources from the Center for High-Performance Computing at the University of Utah. The SDSS website is www.sdss.org.

SDSS-IV is managed by the Astrophysical Research Consortium for the Participating Institutions of the SDSS Collaboration including the Brazilian Participation Group, the Carnegie Institution for Science, Carnegie Mellon University, the Chilean Participation Group, the French Participation Group, Harvard-Smithsonian Center for Astrophysics, Instituto de Astrofísica de Canarias, The Johns Hopkins University, Kavli Institute for the Physics and Mathematics of the Universe (IPMU)/University of Tokyo, the Korean Participation Group, Lawrence Berkeley National Laboratory, Leibniz Institut für Astrophysik Potsdam (AIP), Max-Planck-Institut für Astronomie (MPIA Heidelberg), Max-Planck-Institut für Astrophysik (MPA Garching), Max-Planck-Institut für Extraterrestrische Physik (MPE), National Astronomical Observatories of China, New Mexico State University, New York University, University of Notre Dame, Observatório Nacional/MCTI, The Ohio State University, Pennsylvania State University, Shanghai Astronomical Observatory, United Kingdom Participation Group, Universidad Nacional Autónoma de México, University of Arizona, University of Colorado Boulder, University of Oxford, University of Portsmouth, University of Utah,

University of Virginia, University of Washington, University of Wisconsin, Vanderbilt University, and Yale University.








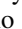






Guoshoujing Telescope (the Large Sky Area Multi-Object Fiber Spectroscopic Telescope, LAMOST) is a National Major Scientific Project built by the Chinese Academy of Sciences. Funding for the project has been provided by the National Development and Reform Commission. LAMOST is operated and managed by the National Astronomical Observatories, Chinese Academy of Sciences.

This work has made use of data from the European Space Agency (ESA) mission Gaia (<https://www.cosmos.esa.int/gaia>), processed by the Gaia Data Processing and Analysis Consortium (DPAC, <https://www.cosmos.esa.int/web/gaia/dpac/consortium>). Funding for the DPAC has been provided by national institutions, in particular the institutions participating in the Gaia Multilateral Agreement.

Facilities: HET, Gaia, SDSS, LAMOST.

Software: astropy (Astropy Collaboration et al. 2013), scipy (Virtanen et al. 2019), tSNE (van der Maaten & Hinton 2008), Turbospectrum (Plez 2012).

ORCID iDs

Keith Hawkins  <https://orcid.org/0000-0002-1423-2174>
 Greg Zeimann  <https://orcid.org/0000-0003-2307-0629>
 Chris Sneden  <https://orcid.org/0000-0002-3456-5929>
 Erin Mentuch Cooper  <https://orcid.org/0000-0002-2307-0146>
 Karl Gebhardt  <https://orcid.org/0000-0002-8433-8185>
 Howard E. Bond  <https://orcid.org/0000-0003-1377-7145>
 Caitlin M. Casey  <https://orcid.org/0000-0002-0930-6466>
 Robin Ciardullo  <https://orcid.org/0000-0002-1328-0211>
 Steven L. Finkelstein  <https://orcid.org/0000-0001-8519-1130>
 Gary J. Hill  <https://orcid.org/0000-0001-6717-7685>
 Matthew Shetrone  <https://orcid.org/0000-0003-0509-2656>
 Donald P. Schneider  <https://orcid.org/0000-0001-7240-7449>
 Matthias Steinmetz  <https://orcid.org/0000-0001-6516-7459>
 J. Craig Wheeler  <https://orcid.org/0000-0003-1349-6538>

References

- Aguado, D. S., Youakim, K., González Hernández, J. I., et al. 2019, *MNRAS*, **490**, 2241
- Ahumada, R., Allende Prieto, C., Almeida, A., et al. 2020, *ApJS*, **249**, 3
- Allende Prieto, C., Sivarani, T., Beers, T. C., et al. 2008, *AJ*, **136**, 2070
- Alvarez, R., & Plez, B. 1998, *A&A*, **330**, 1109
- Anders, F., Chiappini, C., Santiago, B. X., et al. 2018, *A&A*, **619**, A125
- Aoki, W., Beers, T. C., Sivarani, T., et al. 2008, *ApJ*, **678**, 1351
- Astraatmadja, T. L., & Bailer-Jones, C. A. L. 2016, *ApJ*, **832**, 137
- Astropy Collaboration, Robitaille, T. P., Tollerud, E. J., et al. 2013, *A&A*, **558**, A33
- Bailer-Jones, C. A. L. 2015, *PASP*, **127**, 994
- Barnes, J., & Hut, P. 1986, *Natur*, **324**, 446
- Beers, T. C., & Christlieb, N. 2005, *ARA&A*, **43**, 531
- Blanco-Cuaresma, S., Soubiran, C., Heiter, U., & Jofré, P. 2014, *A&A*, **569**, A111
- Boeche, C., Smith, M. C., Grebel, E. K., et al. 2018, *AJ*, **155**, 181
- Bromm, V., & Larson, R. B. 2004, *ARA&A*, **42**, 79
- Buder, S., Asplund, M., Duong, L., et al. 2018, *MNRAS*, **476**, 4513
- Casagrande, L., Wolf, C., Mackey, A. D., et al. 2019, *MNRAS*, **482**, 2770
- De Silva, G. M., Freeman, K. C., Bland-Hawthorn, J., et al. 2015, *MNRAS*, **449**, 2604
- Frebel, A., & Norris, J. E. 2015, *ARA&A*, **53**, 631
- Gaia Collaboration, Brown, A. G. A., Vallenari, A., et al. 2018, *A&A*, **616**, A1
- Gilmore, G., Randich, S., Asplund, M., et al. 2012, *Msngr*, **147**, 25
- Green, J., Schechter, P., Baltay, C., et al. 2012, arXiv:1208.4012
- Gustafsson, B., Edvardsson, B., Eriksson, K., et al. 2008, *A&A*, **486**, 951
- Hawkins, K., Jofré, P., Gilmore, G., & Masseron, T. 2014, *MNRAS*, **445**, 2575
- Hawkins, K., Lucey, M., Ting, Y.-S., et al. 2020, *MNRAS*, **492**, 1164
- Hill, G. J. 2014, *AdOT*, **3**, 265
- Hill, G. J. 2016, in ASP Conf. Ser. 507, Multi-Object Spectroscopy in the Next Decade: Big Questions, Large Surveys, and Wide Fields, ed. I. Skillen, M. Balcells, & S. Trager (San Francisco, CA: ASP), 393
- Hill, G. J., Drory, N., Good, J. M., et al. 2018a, *Proc. SPIE*, **10700**, 107000P
- Hill, G. J., Gebhardt, K., Komatsu, E., et al. 2008, in ASP Conf. Ser. 399, Panoramic Views of Galaxy Formation and Evolution, ed. T. Kodama, T. Yamada, & K. Aoki (San Francisco, CA: ASP), 115
- Hill, G. J., Kelz, A., Lee, H., et al. 2018b, *Proc. SPIE*, **10702**, 107021K
- Home, K. 1986, *PASP*, **98**, 609
- Jofré, P., Travençolo, G., Hawkins, K., et al. 2017, *MNRAS*, **472**, 2517
- Karlsson, T., Bromm, V., & Bland-Hawthorn, J. 2013, *RvMP*, **85**, 809
- Kullback, S. 1959, *Information Theory and Statistics* (New York: Wiley)
- Lee, Y. S., Beers, T. C., Carlin, J. L., et al. 2015, *AJ*, **150**, 187
- Lee, Y. S., Beers, T. C., Sivarani, T., et al. 2008a, *AJ*, **136**, 2022
- Lee, Y. S., Beers, T. C., Sivarani, T., et al. 2008b, *AJ*, **136**, 2050
- Li, H., Tan, K., & Zhao, G. 2018, *ApJS*, **238**, 16
- Lucey, M., Hawkins, K., Ness, M., et al. 2019, *MNRAS*, **488**, 2283
- Luo, A.-L., Zhao, Y.-H., Zhao, G., et al. 2015, *RAA*, **15**, 1095
- Majewski, S. R., Schiavon, R. P., Frinchaboy, P. M., et al. 2017, *AJ*, **154**, 94
- Matijević, G., Chiappini, C., Grebel, E. K., et al. 2017, *A&A*, **603**, A19
- Moffat, A. F. J. 1969, *A&A*, **3**, 455
- Plez, B. 2012, Turbospectrum: Code for spectral synthesis, Astrophysics Source Code Library, ascl:1205.004
- Ramsey, L. W., Sebring, T. A., & Sneden, C. A. 1994, *Proc. SPIE*, **2199**, 31
- Roederer, I. U., Preston, G. W., Thompson, I. B., et al. 2014, *AJ*, **147**, 136
- Rogers, B., Ferreras, I., Peletier, R., & Silk, J. 2010, *MNRAS*, **402**, 447
- Ruchti, G. R., Fulbright, J. P., Wyse, R. F. G., et al. 2010, *ApJL*, **721**, L92
- Sakari, C. M., Placco, V. M., Farrell, E. M., et al. 2018, *ApJ*, **868**, 110
- Smolinski, J. P., Lee, Y. S., Beers, T. C., et al. 2011, *AJ*, **141**, 89
- Starkenburgh, E., Martin, N., Youakim, K., et al. 2017, *MNRAS*, **471**, 2587
- Steinmetz, M., Matijević, G., Enke, H., et al. 2020, *AJ*, **160**, 82
- Steinmetz, M., Zwitter, T., Siebert, A., et al. 2006, *AJ*, **132**, 1645
- Ting, Y.-S., Conroy, C., Rix, H.-W., & Cargile, P. 2017, *ApJ*, **843**, 32
- van der Maaten, L. 2014, *JMLR*, **15**, 3221
- van der Maaten, L., & Hinton, G. 2008, *JMLR*, **9**, 2579
- Virtanen, P., Gommers, R., Oliphant, T. E., et al. 2019, *Nat. Method.*, **17**, 261
- Wang, R., Luo, A. L., Chen, J. J., et al. 2019, *ApJS*, **244**, 27
- Xiang, M., Ting, Y.-S., Rix, H.-W., et al. 2019, *ApJS*, **245**, 34
- Xiang, M.-S., Liu, X.-W., Yuan, H.-B., et al. 2017, *MNRAS*, **467**, 1890
- Xu, S.-Y., Zhang, H.-W., & Liu, X.-W. 2013, *RAA*, **13**, 313
- Yanny, B., Rockosi, C., Newberg, H. J., et al. 2009, *AJ*, **137**, 4377
- Yong, D., Norris, J. E., Bessell, M. S., et al. 2013, *ApJ*, **762**, 26
- York, D. G., Adelman, J., Anderson, J. E., Jr., et al. 2000, *AJ*, **120**, 1579
- Zucker, S. 2003, *MNRAS*, **342**, 1291